Article

Not peer-reviewed version

Size Uniformity of CsPbBr3 Perovskite Quantum Dots via Manganese-Doping

Mi Zhang , Xue Han , Changgang Yang , Guofeng Zhang * , Wenli Guo , Jialu Li , Zhihao Chen , Bin Li , Ruiyun Chen , Chengbing Qin , Jianyong Hu , Zhichun Yang , Ganying Zeng , Liantuan Xiao * , Suotang Jia

Posted Date: 9 July 2024

doi: 10.20944/preprints202407.0749.v1

Keywords: $CsPbBr_3$ perovskite quantum dots; manganese-doping; size uniformity; single quantum-dot spectroscopy; narrow-linewidth doi:10.20944/preprints202407.0749.v1

Article

Size Uniformity of $CsPbBr_3$ Perovskite Quantum Dots via Manganese-Doping

Mi Zhang [1], Xue Han [1], Changgang Yang [1], Guofeng Zhang [1,*], Wenli Guo [1], Jialu Li [1], Zhihao Chen [1], Bin Li [1], Ruiyun Chen [1], Chengbing Qin [1], Jianyong Hu [1], Zhichun Yang [1], Ganying Zeng [1], Liantuan Xiao [1,2,*] and Suotang Jia [1]

[1] State Key Laboratory of Quantum Optics and Quantum Optics Devices, Institute of Laser Spectroscopy, Collaborative Innovation Center of Extreme Optics, Shanxi University, Taiyuan, 030006, China
[2] College of Physics, Taiyuan University of Technology, Taiyuan, Shanxi 030006, China
* Correspondence: guofeng.zhang@sxu.edu.cn (G. Z.); xlt@sxu.edu.cn (L. X.)

Abstract: The achievement of size uniformity and monodispersity in perovskite quantum dots (QDs) re-quires the implementation of precise temperature control and the establishment of optimal re-action conditions. Nevertheless, the accurate control of a range of reaction variables represents a considerable challenge. This study addresses the aforementioned challenge by employing manganese (Mn) doping to achieve size uniformity in $CsPbBr_3$ perovskite QDs without the necessity for precise control of the reaction conditions. By optimizing the Mn:Pb ratio, it is possible to successfully dope $CsPbBr_3$ QDs with appropriate concentrations of Mn^{2+} and achieve a uniform size distribution. The spectroscopic measurements on single QDs indicate that the appropriate Mn^{2+} concentrations can result in a narrower spectral linewidth, a longer photoluminescence (PL) lifetime, and a reduced biexciton Auger recombination rate, thus positively affecting the PL properties. This study not only simplifies the size control of perovskite QDs, but also demonstrates the potential of Mn-doped $CsPbBr_3$ QDs for narrow linewidth light-emitting diode applications.

Keywords: $CsPbBr_3$ perovskite quantum dots; manganese-doping; size uniformity; single quantum-dot spectroscopy; narrow-linewidth

---

1. Introduction

Cesium lead halide ($CsPbX_3$, where X = Cl, Br, or I) perovskite quantum dots (QDs) display a range of advantageous properties, including high photoluminescence (PL) quantum yields, tunable PL spectra, high defect tolerance, and large carrier diffusion lengths [1-4]. These excellent properties have led to considerable potential for $CsPbX_3$ perovskite QDs in a wide range of applications, including light-emitting diodes (LEDs) [5,6], photovoltaics [7], lasers [8,9], photodetectors [10,11], and quantum light sources [12]. Nevertheless, the properties and applications of nanoscale perovskite QDs are strongly dependent on their size uniformity and monodispersity. As the size of the QDs is smaller than their Bohr diameter, the energy levels are quantized due to quantum confinement effects. As the size of the QD decreases, the confinement of the carriers becomes stronger, leading to an increase in the energy spacing between the discrete energy levels [13,14]. Consequently, the optical and electronic properties of QDs are highly sensitive to their size. The non-uniformity of the size of QDs typically leads to the broadening of the PL spectra, which in turn affects the performance of QD-based devices [15-18]. Consequently, size uniformity is of paramount importance in determining the performance, stability, and controllability of QD-based applications. This ensures consistency in optical, electronic, and assembly properties, thereby improving the functionality and reliability of devices in a range of fields. Nevertheless, the production of perovskite QDs with high size uniformity using colloidal methods remains a significant challenge.

A variety of synthesis methods and strategies have been employed to achieve size uniformity and monodispersity in perovskite QDs. For example, precursor stoichiometry control has been used to precisely tune precursor ratios to influence nucleation and growth kinetics, resulting in uniform perovskite QD sizes [19,20]. The precise control of temperature and reaction time has been employed to regulate synthesis conditions, resulting in the formation of smaller, more uniform perovskite QDs [21,22]. Furthermore, solvent engineering has been utilized to optimize solubility and growth kinetics, thereby improving size control [23,24]. The use of ligands such as oleic acid or oleylamine in surfactant engineering has been employed to stabilize perovskite QDs and enhance size uniformity [25,26]. However, maintaining precise temperature control and appropriate reaction conditions can be challenging, resulting in variations in perovskite QD size and uniformity.

In this study, we demonstrate the successful achievement of size uniformity and monodispersity of $CsPbBr_3$ perovskite QDs through the incorporation of manganese (Mn) doping. This method does not necessitate the precise control of various reaction conditions for the synthesis of $CsPbBr_3$ perovskite QDs. It has been demonstrated that Mn doping in perovskite QDs can stabilize the crystal structure, effectively reduce the defect density and improve the lattice ordering [26]. By optimizing the Mn:Pb ratio in the precursor, it was possible to successfully introduce appropriate concentrations of Mn^{2+} into the $CsPbBr_3$ perovskite QDs. The introduction of Mn^{2+} greatly optimizes the size distribution of $CsPbBr_3$ perovskite QDs. Single QD spectroscopy measurements demonstrate that the incorporation of Mn^{2+} at appropriate concentrations has a positive effect on the PL properties of $CsPbBr_3$ perovskite QDs.

2. Materials and Methods

All materials were purchased from Aladdin and used as received without further purification. The materials used in the experiments include cesium carbonate (Cs_2CO_3, 99.9%, metals basis), lead bromide ($PbBr_2$, 99.0%), zinc bromide ($ZnBr_2$, 99.9%, metals basis), manganese (II) bromide ($MnBr_2$, 98.0%), oleylamine (OAm, C18:80-90%), oleic acid (OA, AR), 1-octadecene (ODE, >90.0%(GC)), hexane (>99%(GC)).

In this study, $CsPbBr_3$ perovskite QDs were synthesized by suitably modifying the previously reported hot injection synthesis method [19]. Stoichiometric mixtures of different ratios of $ZnBr_2$ and $MnBr_2$ were used for the synthesis of Mn-doped $CsPbBr_3$ perovskite QDs with different doping concentrations. The Cs precursor solution was prepared by reacting 0.25 g of Cs_2CO_3 powder with 0.9 mL of OA and 9 mL of ODE in a 50 mL three-necked flask. This reaction was conducted at 150 °C under a nitrogen (N_2) atmosphere. A separate solution was then prepared by mixing 75 mg of $PbBr_2$, together with specific proportions of $ZnBr_2$ and $MnBr_2$, with 5 mL of ODE, 2 mL of OA, and 2 mL of OAm in a separate 50 mL round-bottomed three-necked flask. The aforementioned mixture was maintained at 120 °C under an N_2 atmosphere for one hour to ensure thorough mixing and solubilization. Once the requisite temperature was reached, 0.4 mL of the previously prepared Cs precursor solution was rapidly injected into the flask containing the $PbBr_2$ mixture. This injection initiated the nucleation and subsequent growth of the $CsPbBr_3$ perovskite QDs. To promptly terminate the reaction, the flask was immersed in an ice bath after 5 seconds. After the reaction, the $CsPbBr_3$ perovskite QDs were separated from the reaction mixture by high-speed centrifugation. Methyl acetate was used as an antisolvent to precipitate the perovskite QDs, which were then redispersed in hexane. Unreacted salts and impurities were removed as precipitates through centrifugation at 4000 rpm, and the supernatant, containing the dispersed perovskite QDs, was collected for further use.

For single QD measurements, the hexane solution of perovskite QDs was mixed with 1 wt.% polystyrene solution. The mixture was then spincoated onto clean glass coverslips at 3000 rpm for one minute to form a polystyrene film to protect the perovskite QDs. The size of the perovskite QDs was measured from the TEM image using a JEM-2100 microscope. The absorption and PL emission spectra of the perovskite QDs in hexane were measured using a PerkinElmer Lambda 950 UV–VISNIR spectrometer and a Cary Eclipse Fluorescence Spectrophotometer, respectively. X-ray diffraction (XRD) patterns of the perovskite QDs were obtained using a D2 PHASER diffractometer. The elemental concentrations of Mn-doped perovskite QDs were determined using a NexION350 series inductively coupled plasma mass spectrometer (ICP-MS).

Preprints.org (www.preprints.org) | NOT PEER-REVIEWED | Posted: 9 July 2024 doi:10.20944/preprints202407.0749.v1

A confocal fluorescence microscopy system was home-built to collect PL photons emitted from single QDs [27,28]. A pulsed laser emitting at 439 nm (EXW-12, NKT) with a pulse duration of 50 to 100 ps and a repetition rate of 5 MHz was used for excitation. The system incorporated an Olympus oil immersion objective with a high magnification of 100× and a numerical aperture (NA) of 1.3, which not only facilitates precise focusing of the laser beam onto the QD samples, but also efficiently collects the emitted PL photons. The collected PL photons were initially filtered through a dichroic mirror (Semrock) and a high-pass filter (Semrock) to eliminate any background noise that might otherwise interfere with the analysis. Subsequently, a spatial filtering step using a 100 μm pinhole was employed to reject out-of-focus photons, thereby ensuring that only the desired PL photons were processed. A 50/50 beam-splitter cube was then used to divide the filtered PL photons into two equal beams. Each beam was then detected by a highly sensitive single-photon avalanche diode detector (SPCM-AQR-15, PerkinElmer), which is capable of rapidly responding to individual photons. The detected signals were accurately recorded by a time-tagged time-resolved (TTTR) time-correlated single-photon counting (TCSPC) data acquisition card (HydraHarp 400, PicoQuant), which provides a temporal resolution of 16 ps. Of note, all measurements were conducted at room temperature in order to ensure reproducibility and comparability with other experiments. The described setup and procedures adhere to standard practices in fluorescence microscopy and single-photon detection, thus ensuring reliability and accuracy data obtained for the investigation of the PL properties of perovskite QDs.

3. Results and Discussion

The synthesis of Mn-doped $CsPbBr_3$ perovskite QDs was successfully accomplished using $MnBr_2$ as a dopant. The doping concentrations of the QDs were 1.3%, 3.9%, and 5.8%, with the undoped QDs serving as a control. The Mn^{2+} concentration was accurately determined by inductively coupled plasma mass spectrometry (ICP-MS) analysis, as shown in Table S1. Taking the undoped and 1.3% Mn-doped $CsPbBr_3$ perovskite QDs as examples, the transmission electron microscopy (TEM) images presented in Figure 1a,b illustrate the distinct morphological discrepancies between the undoped and 1.3% Mn-doped perovskite QDs. Following the incorporation of 1.3% Mn doping, notable improvements in both the size distribution and morphology of the perovskite QDs were observed. In particular, these QDs exhibit a strikingly uniform size distribution, with a significant reduction in the full width at half maximum (FWHM) of the size distribution from 2 nm to 1.2 nm (Figure 1c,d), which highlights the high level of control over the size uniformity by Mn doping. Furthermore, the original cubic morphology becomes more distinct and well-defined, indicating an improvement in crystallinity. At the same time, this optimization is reflected in the emission spectrum of the perovskite QDs, where the FWHM of the emission spectrum is significantly narrowed from 34.5 nm to 24.1 nm (Figure 1e), representing a 30.3% reduction compared to the original width. This indicates a more homogeneous energy distribution and improved optical properties of the doped perovskite QDs. These improvements can be attributed to the effective regulation of surface defects on the QD surfaces by Mn doping. During the conventional perovskite QDs growth process, the formation of surface defects with high free energy is a consequence of the presence of unpaired chemical bonds on the QD surfaces. In contrast, Mn doping has the effect of reducing these defects by increasing the defect formation energy while avoiding the introduction of deep traps into the band gap. This not only improves the short-range order of the crystal lattice, but also brings the local structural order closer to an ideal state of uniformity [26,29]. A significant reduction in the average edge length of the perovskite QDs was also observed, from 6.41 nm to 6.08 nm (Figure 1c,d). This reduction can be attributed to the substitution of Pb^{2+}, which has a larger ionic radius, by the equivalent but smaller Mn^{2+}. The substitution of Pb^{2+} by Mn^{2+} results in a contraction of the lattice, which causes a monotonic shift of the peaks in the X-ray diffraction (XRD) patterns by 0.11° towards higher angles, as shown in Figure 1f,g. Furthermore, a slight redshift in the position of the PL emission peak can be observed (Figure 1e). This redshift is attributed to the enhancement of the coordination field around Mn^{2+} due to lattice contraction, which leads to a narrowing of the band gap between the $^4T_1$ and $^6A_1$ energy levels [30]. The aforementioned observations provide compelling evidence that the perovskite QDs have been successfully doped [31].

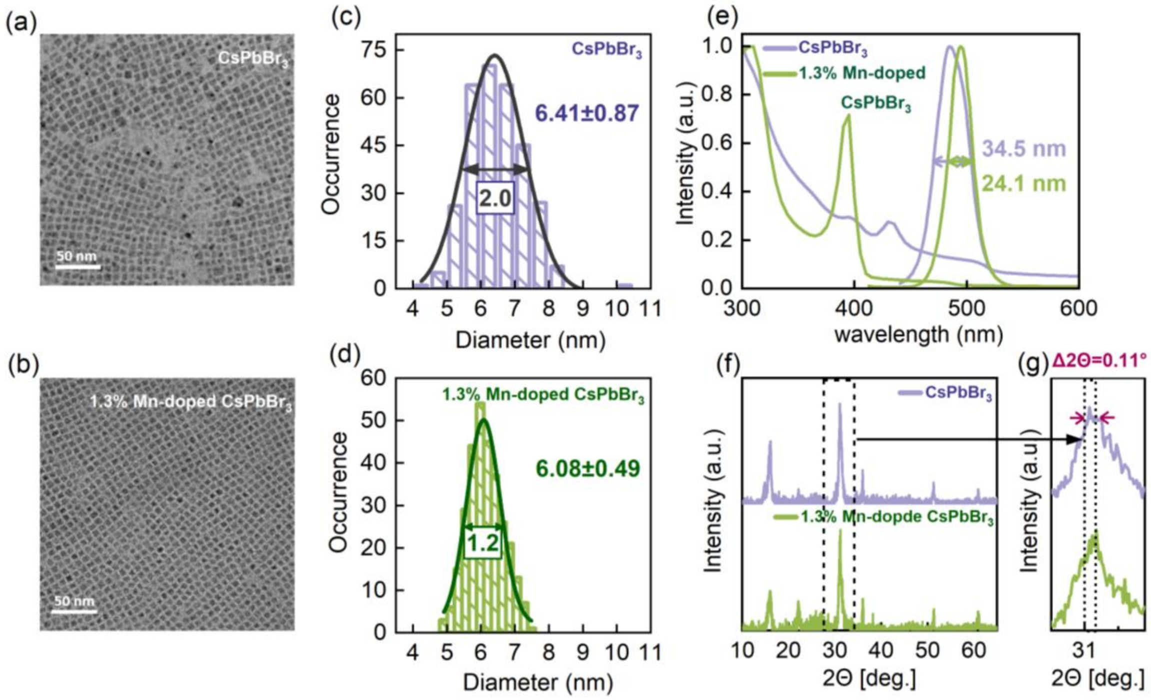

Figure 1. Morphological, spectral, and structural characterization of undoped and 1.3% Mn-doped $CsPbBr_3$ perovskite quantum dots (QDs). (a, b) Transmission electron microscopy (TEM) images of undoped and Mn-doped $CsPbBr_3$ perovskite QDs. (c, d) Histograms depicting the distribution of edge lengths for undoped and Mn-doped perovskite QDs. (e) Absorption and PL emission spectra of undoped and Mn-doped perovskite QDs, demonstrating that Mn-doped perovskite QDs exhibit a narrower linewidth. (f) X-ray diffraction (XRD) patterns of perovskite QDs with different Mn doping concentrations, demonstrating the preservation of the cubic phase upon Mn doping. (g) A magnified view shows a subtle but monotonic shift in the XRD peak towards higher 2θ angles, indicating a progressive contraction of the lattice with Mn doping.

As the ratio of $MnBr_2$ increases from 1.3% to 3.9%, a slight blue shift in the absorption edge can be observed, accompanied by a corresponding shift in the PL peak from 496.6 nm to 486.6 nm (Figures S1d, g). As the ratio of $MnBr_2$ exceeds 3.9%, the size distribution and morphology of the perovskite QDs deteriorate, resulting in a reverse redshift in the characteristic spectra (Figures S1j, k). Furthermore, it was observed that the Mn-doped perovskite QDs did not exhibit Mn-related PL in the visible spectral region at room tem-perature due to the low energy of the excitonic transition [30,32,33].

In order to investigate the impact of doping on $CsPbBr_3$ perovskite QDs, we conducted single-dot PL spectroscopy on undoped and 1.3% Mn-doped $CsPbBr_3$ perovskite QDs under identical excitation conditions. The excitation condition $\langle N \rangle$ represents the average number of photons absorbed per QD per pulse. $\langle N \rangle = \sigma \cdot j_{exc}$, where j_{exc} is the perpulse photon fluence and σ is the QD absorption cross section [4,34]. The estimation of $\langle N \rangle$ and calculation of the absorption cross section σ can be found in Supporting Information. The average values of σ for the undoped and 1.3% Mn-doped $CsPbBr_3$ perovskite QDs are 3.52×10^{-14} cm^2 and 2.97×10^{-14} cm^2, respectively (Figure S2), which is consistent with the findings of previous research [4]. Figure 2a,2b illustrate the typical PL intensity trajectories for single undoped and 1.3% Mn-doped perovskite QDs under low excitation ($\langle N \rangle = 0.2$). The corresponding PL intensity histograms are shown in the right panels. From the figures, it can be observed that the PL intensity trajectory of the single 1.3% Mn-doped QD remains essentially unchanged compared to that of the undoped QD. However, as the doping concentration increases, the PL trajectories of the perovskite QDs deteriorate, exhibiting a decrease in intensity and an increase in blinking (Figure S3). By applying a single exponential fit to each 10 ms time bin of the PL trajectories, fluorescence lifetime-intensity distribution (FLID) maps can be derived, which provide valuable insights into the PL properties of the QDs [35,36]. Prior to and following doping, the PL intensity of single $CsPbBr_3$ perovskite QDs exhibits a linear correlation with their lifetime, indicating that PL blinking in both undoped and Mn-doped QDs is primarily dominated by band-edge carrier (BC) blinking (Figure 2c,d). This implies that the moderate amount of Mn doping did not alter the blinking mechanism of the perovskite QDs.

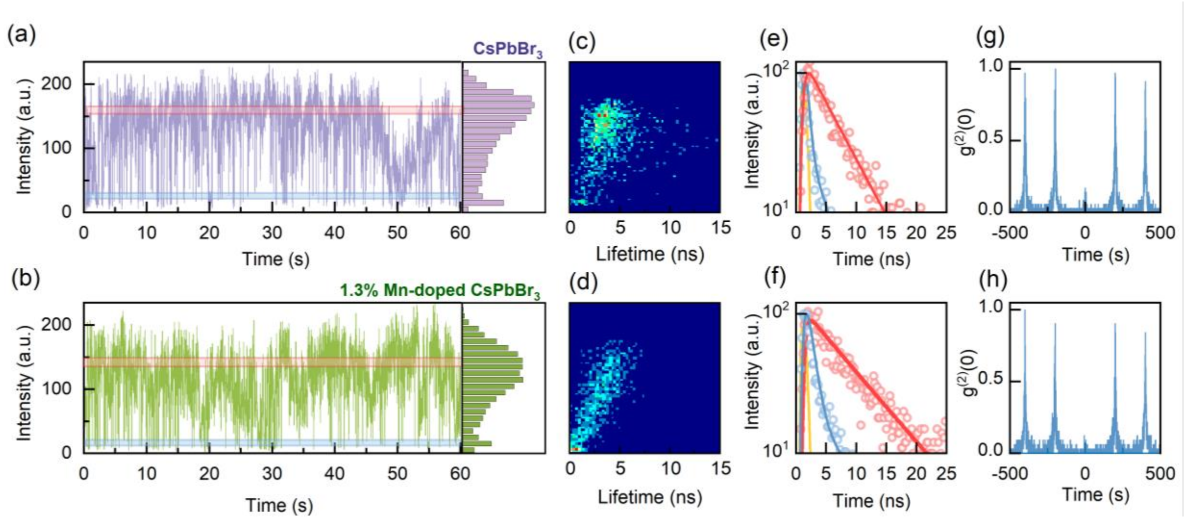

Figure 2. (a, b) Typical PL intensity time trajectories for single undoped and 1.3% Mn-doped $CsPbBr_3$ perovskite QDs. Corresponding PL intensity histograms are presented in the right panels. (c, d) Corresponding fluorescence lifetime-intensity distribution (FLID) maps. The color change from blue to red indicates an increase in the probability of occurrence of a given state in the intensity-lifetime space. (e, f) Corresponding PL decay trajectories obtained from the bright- and dim-state PL regions marked in respective colors on the PL intensity trajectories of (a) and (b). The solid red and blue lines represent mono-exponential fits, and the solid yellow lines in the figures represent the instrument response function (IRF) of the system. (g, h) Corresponding second-order correlation function ($g^{(2)}$) curves of the bright-state PL regions for single undoped and 1.3% Mn-doped $CsPbBr_3$ perovskite QDs.

The corresponding PL decay trajectories, extracted from the bright- and dim-state PL regions, are presented in Figure 2e,f, respectively. The decay curves can be fitted by monoexponential functions to obtain the bright- and dim-state lifetimes. The radiative lifetime scaling can be calculated based on the bright- and dim-state lifetimes and the corresponding PL intensities of the bright- and dim-state. The radiative lifetime scaling for both undoped and 1.3% Mn-doped $CsPbBr_3$ perovskite QDs is approximately 1.0 (details of the scaling calculations can be found in the Supporting Information), which further confirms that both undoped and Mn-doped perovskite QDs adhere to the BC blinking mechanism [37,38]. This BC blinking behavior indicates that the blinking of undoped and Mn-doped perovskite QDs is primarily attributed to the surface shallow trap states. Given the analogous energy level structure of the Mn and $CsPbBr_3$ perovskite QDs, doping Mn^{2+} does not introduce deep trap states, and thus does not alter the carrier trapping and detrapping rates. The corresponding second-order correlation function ($g^{(2)}$) curves depicted in Figure 2g,h show very low values of $g^{(2)}(0)$, well below 0.5. This observation suggests that the investigated perovskite QDs are single QDs [39], and also indicates that Mn doping does not appear to alter the photon statistical properties of the QDs.

In order to gain further insight into the impact of Mn doping on $CsPbBr_3$ perovskite QDs, a statistical analysis was conducted on the single-exciton lifetimes of both single undoped and Mn-doped $CsPbBr_3$ perovskite QDs. The single-exciton lifetime can be determined by fitting the bright state of the PL intensity trajectory. The histograms of single-exciton lifetimes are presented in Figure 3a,b, and the results were obtained from approximately 100 QDs in each case. The average lifetime value of 1.3% Mn-doped $CsPbBr_3$ perovskite QDs is 5.37 ns, which is larger than the average lifetime value of undoped $CsPbBr_3$ perovskite QDs (4.93 ns). This increase in the lifetime value indicates that the doping of Mn^{2+} favors the suppression of defect recombination [40].

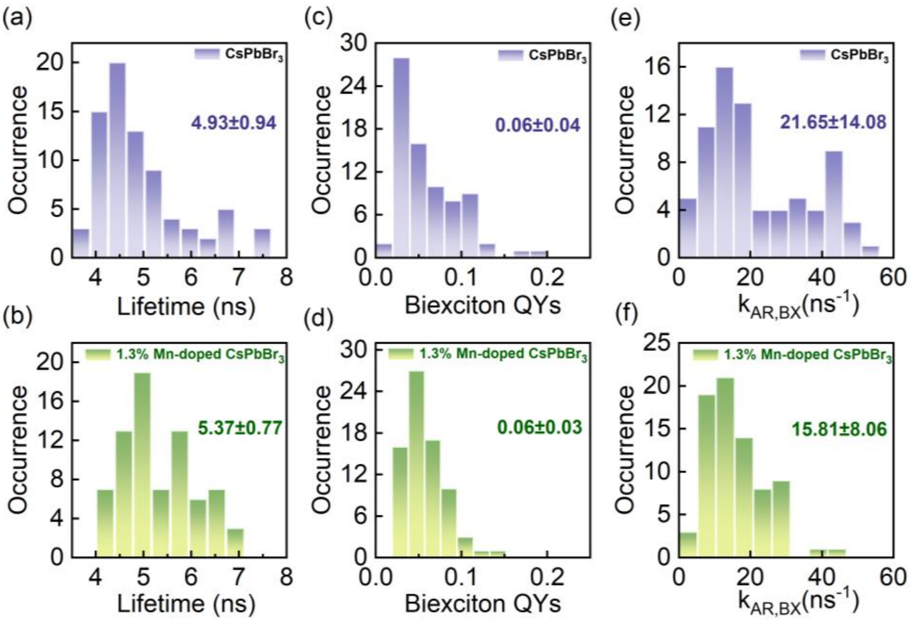

Figure 3. (a, b) Histograms of single exciton lifetimes for single undoped and 1.3% Mn-doped $CsPbBr_3$ perovskite QDs. (c, d) Histograms of biexciton quantum yields (QYs) for single undoped and Mn-doped $CsPbBr_3$ perovskite QDs. (e, f) Histograms of biexciton Auger recombination rates ($k_{AR,BX}$) for single undoped and Mn-doped $CsPbBr_3$ perovskite QDs.

Furthermore, we conducted a detailed investigation into the impact of doping on the biexciton quantum yields (QYs) and biexciton Auger recombination rates ($k_{AR,BX}$) in perovskite QDs. In the case of weak excitation conditions with $\langle N \rangle = 0.2$, the biexciton quantum yields (QYs) can be calculated using the Eq. 1 [41,42].

$$QY_{BX} = g^{(2)}(0) \times \mathrm{QY}_X \qquad (1)$$

Where QY_{BX} and QY_X are the biexciton QY and single-exciton QY, respectively. It is assumed that the single-exciton QY of the on-state PL intensity trajectory is unity for single QDs [41]. According to the values of $g^{(2)}(0)$, the biexciton QYs of single undoped and Mn-doped $CsPbBr_3$ perovskite QDs can be obtained by Eq. 1. The histograms of biexciton QYs in the two cases are presented in Figure 3c,d, respectively, and the average values are calculated to be 0.06 and 0.06, respectively. This suggests that Mn doping has a minimal impact on the biexciton QYs of perovskite QDs.

When the excitation condition $\langle N \rangle \ll 1$, the relationship of $g^{(2)}(0)$ to the biexciton and single-exciton lifetimes of a single perovskite QD can be expressed by the Eq. 2 [16,42,43].

$$g^{(2)}(0) = 4\frac{\tau_{BX}}{\tau_X} \qquad (2)$$

Where τ_{BX} and τ_X are the biexciton and single-exciton lifetimes, respectively. The biexciton QY can be expressed by Eq. 3 [42].

$$QY_{BX} = \frac{k_{r,BX}}{k_{r,BX} + k_{AR,BX}} = \frac{k_{r,BX}}{1/\ \tau_{BX}} \tag{3}$$

Where $k_{r,BX}$ and $k_{AR,BX}$ represent the biexciton radiative rate and biexciton Auger recombination rate, respectively. According to Eqs. 2 and 3, $k_{AR,BX}$ can be obtained. Histograms of $k_{AR,BX}$ for single undoped and Mn-doped $CsPbBr_3$ perovskite QDs are shown in Figure 3e,f. The $k_{AR,BX}$ values for undoped perovskite QDs exhibit a relatively wide distribution, reflecting the non-uniform size distribution of the undoped QDs (Figure 3e). The mean value of $k_{AR,BX}$ is 21.65 ns^{-1}. In contrast, the distribution of $k_{AR,BX}$ of Mn-doped perovskite QDs is more concentrated (Figure 3f). This is primarily attributed to the enhancement of their size uniformity and the significant reduction in size dispersion achieved by Mn doping. The average value of $k_{AR,BX}$ is 15.81 ns^{-1} for the Mn-doped QDs, which is smaller than that of the undoped QDs. This evidence demonstrates that the incorporation of Mn effectively mitigates the discreteness of the $k_{AR,BX}$. The reduction in the $k_{AR,BX}$ achieved by minimizing non-radiative recombination processes leads to an increase in the radiative recombination fraction. At the same time, the reduced $k_{AR,BX}$ indicates that the quantum confinement on the carriers is reduced, creating favorable conditions for the overall enhancement of LED device performance.

One of the key challenges in the advancement of QD LED (QLED) technology is the relatively wide emission spectra, which affects the color purity of the emitted light from LEDs [44,45]. To further validate the feasibility of Mn-doped $CsPbBr_3$ perovskite QDs for LED applications, we employed undoped and 1.3% Mn-doped $CsPbBr_3$ perovskite QDs as down-conversion phosphors. The $CsPbBr_3$ perovskite QDs were thoroughly mixed with a 1wt% polystyrene (PS)-toluene solution to improve the stability. The resulting mixture was then applied to a 395 nm UV chip and allowed to dry in air for one hour, resulting in the fabrication of the QLED device. As illustrated in Figure 4a,b, at a driving voltage of 3 V, the FWHM of the light emission of the QLED based on Mn-doped $CsPbBr_3$ perovskite QDs is 24.3 nm, which is smaller than that of the undoped QDs (31.5 nm). The green light purity of the two QLEDs is expressed in CIE coordinates as (0.26, 0.54) for the undoped perovskite QDs and (0.18, 0.62) for the 1.3% Mn-doped perovskite QDs, as shown in Figure 4c. Notably, the QLED based on Mn-doped QDs exhibit color coordinates that are closer to the ideal green LED coordinates in the 1931 color space (0.170, 0.797) [46] and exhibit a higher degree of color purity, which highlights the great potential of doped perovskite QDs for LED fabrication.

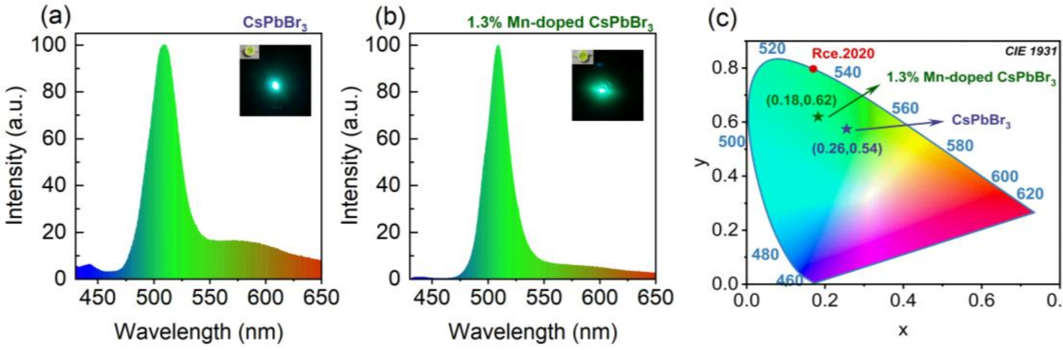

Figure 4. (a, b) Light-emitting diode (LED) emission spectra of the undoped and 1.3% Mn-doped $CsPbBr_3$ perovskite QDs. Insets: Optical images corresponding to the LED. (c) Chromaticity coordinates.

4. Conclusions

Mn-doped $CsPbBr_3$ perovskite QDs have been successfully prepared by introducing an appropriate amount of Mn^{2+} into the QDs. The study demonstrates that Mn doping significantly increases the defect formation energy, which promotes the formation of nearly uniform local structural order in the perovskite QDs, leading to improved size uniformity and monodispersity. The FWHM of size distribution of the perovskite QDs was reduced from 2 nm to 1.2 nm, with a 30.3% reduction in the PL emission linewidth compared to the undoped QDs, indicating a more homogeneous energy distribution and improved optical properties. The study reveals that the optimal doping effect is achieved when the Mn doping concentration of perovskite QDs is set at 1.3% among four different doping concentrations. This doping process does not result in the introduction of deep trap states within the band gap and instead improves the size uniformity. Furthermore, the improvement in PL properties is evidenced by the narrowing of spectral linewidths, the increase in PL lifetime and the reduction of Auger recombination rate. Additionally, a 23% reduction in linewidth was observed for 1.3% doped QLEDs, with a CIE color coordinate of (0.18, 0.62) that is closer to the ideal coordinates for green LEDs, further demonstrating their potential for LED applications. This work offers an effective strategy for enhancing the color purity of perovskite QD-based LEDs.

Supplementary Materials: The following supporting information can be downloaded at the website of this paper posted on Preprints.org. Estimation of $\langle N\rangle$ and calculation of the absorption cross section σ; calculations of radiative lifetime scaling. Figure S1: Morphological, spectral, and structural characterization of undoped and Mn-doped $CsPbBr_3$ perovskite QDs with different doping ratios; Figure S2: Histogram of absorption cross sections of undoped and 1.3% Mn-doped $CsPbBr_3$ perovskite QDs. Figure S3: Typical PL intensity time trajectory for single $CsPbBr_3$ perovskite QDs with different doping ratios; Table 1: ICP-OES quantitative element scanning analysis of Mn-doped $CsPbBr_3$ synthesized with $PbBr_2$ as Pb^{2+} source and $MnBr_2$ as doping precursor.

Author Contributions: Conceptualization, Guofeng Zhang and Liantuan Xiao; data curation, Mi Zhang, Xue Han; formal analysis, Changgang Yang, Jialu Li, Wenli Guo, Zhihao Chen, Bin Li; visualization, Mi Zhang, Guofeng Zhang; funding acquisition, Guofeng Zhang, Ruiyun Chen, Chengbing Qin, Jianyong Hu, Zhichun Yang, Ganying Zeng, Liantuan Xiao, and Suotang Jia; writing-original draft, Mi Zhang and Guofeng Zhang; writing-review & editing, Guofeng Zhang, Ruiyun Chen, Chengbing Qin, Jianyong Hu, Zhichun Yang, Ganying Zeng, Liantuan Xiao, and Suotang Jia. All authors have read and agreed to the published version of the manuscript.

Funding: The authors acknowledge financial support from the National Key Research and De-velopment Program of China (No. 2022YFA1404201), the Natural Science Foundation of China (Nos. 62127817, U22A2091, U23A20380, 62075120, 62222509, 62075122, 62205187, 62105193, 62305201 and 62305200), NSFC-STINT (No. 62011530133), Program for Changjiang Scholars and Innovative Research Team (No. IRT_17R70), China Postdoctoral Science Foundation (No. 2022M722006), Fundamental Research Program of Shanxi Province (No. 202303021222031, 202103021223032, 202103021223254), Shanxi Province Science and Technology Innovation Talent Team (No. 202204051001014), Shanxi Province Science and Technology Major Special Project (No. 202201010101005), Science and Technology Cooperation Project of Shanxi Province (202104041101021), Shanxi "1331 Project", and 111 project (No. D18001).

Data Availability Statement: Data underlying the results are contained within the article or Supplementary Materials.

Conflicts of Interest: The authors declare no conflicts of interest.

References

1. Tang, Y.; Tang, S.; Luo, M.; Guo, Y.; Zheng, Y.; Lou, Y.; Zhao, Y. All-inorganic lead-free metal halide perovskite quantum dots: progress and prospects. *Chem. Commun.* **2021**, *57*, 7465-7479.
2. Wu, X.; Ji, H.; Yan, X.; Zhong, H. Industry outlook of perovskite quantum dots for display applications. *Nat. Nanotechnol.* **2022**, *17*, 813-816.
3. Li, B.; Zhang, G.; Gao, Y.; Chen, X.; Chen, R.; Qin, C.; Hu, J.; Wu, R.; Xiao, L.; Jia, S. Single quantum dot spectroscopy for exciton dynamics. *Nano Res.* **2024**, doi: 10.1007/s12274-12024-16504-x.
4. Li, B.; Huang, H.; Zhang, G.; Yang, C.; Guo, W.; Chen, R.; Qin, C.; Gao, Y.; Biju, V.P.; Rogach, A.L.; et al. Excitons and biexciton dynamics in single $CsPbBr_3$ perovskite quantum dots. *J. Phys. Chem. Lett.* **2018**, *9*, 6934-6940.

5. Li, Y.; Du, K.; Zhang, M.; Gao, X.; Lu, Y.; Yao, S.; Li, C.; Feng, J.; Zhang, H. Tunable ultra-uniform Cs_4PbBr_6 perovskites with efficient photoluminescence and excellent stability for high-performance white light-emitting diodes. *J. Mater. Chem.* **2021**, *9*, 12811-12818.
6. He, X.; Li, T.; Liang, Z.; Liu, R.; Ran, X.; Wang, X.; Guo, L.; Pan, C. Enhanced cyan photoluminescence and stability of $CsPbBr_3$ quantum dots via surface engineering for white light-emitting diodes. *Adv. Opt. Mater.* **2024**, *12*, 2302726.
7. Liu, Y.; Yuan, S.; Zheng, H.; Wu, M.; Zhang, S.; Lan, J.; Li, W.; Fan, J. Structurally dimensional engineering in perovskite photovoltaics. *Adv. Energy Mater.* **2023**, *13*, 2300188.
8. Chen, L.J.; Dai, J.H.; Lin, J.D.; Mo, T.S.; Lin, H.P.; Yeh, H.C.; Chuang, Y.C.; Jiang, S.A.; Lee, C.R. Wavelength-tunable and highly stable perovskite-quantum-dot-doped lasers with liquid crystal lasing cavities. *ACS Appl. Mater. Interfaces* **2018**, *10*, 33307-33315.
9. Nguyen, T.; Tan, L.Z.; Baranov, D. Tuning perovskite nanocrystal superlattices for superradiance in the presence of disorder. *J. Chem. Phys.* **2023**, *159*, 204703.
10. Lin, L.; Liu, Y.; Wu, W.; Huang, L.; Zhu, X.; Xie, Y.; Liu, H.; Zheng, B.; Liang, J.; Sun, X. Self-powered perovskite photodetector arrays with asymmetric contacts for imaging applications. *Adv. Electron. Mater.* **2023**, *9*, 2300106.
11. Pan, X.; Ding, L. Application of metal halide perovskite photodetectors. *J. Semicond.* **2022**, *43*, 020203.
12. Ma, J.; Zhang, J.; Horder, J.; Sukhorukov, A.A.; Toth, M.; Neshev, D.N.; Aharonovich, I. Engineering quantum light sources with flat optics. *Adv. Mater.* **2024**, *36*, 2313589.
13. Kulkarni, S.A.; Yantara, N.; Tan, K.S.; Mathews, N.; Mhaisalkar, S.G. Perovskite nanostructures: leveraging quantum effects to challenge optoelectronic limits. *Mater. Today* **2020**, *33*, 122-140.
14. Lu, X.; Hou, X.; Tang, H.; Yi, X.; Wang, J. A high-quality CdSe/CdS/ZnS quantum-dot-based FRET aptasensor for the simultaneous detection of two different Alzheimer's disease core biomarkers. *Nanomaterials* **2022**, *12*, 4031.
15. Chen, M.; Shen, G.; Guyot-Sionnest, P. Size distribution effects on mobility and intraband gap of HgSe quantum dots. *J. Phys. Chem. C* **2020**, *124*, 16216-16221.
16. Yang, C.; Zhang, G.; Gao, Y.; Li, B.; Han, X.; Li, J.; Zhang, M.; Chen, Z.; Wei, Y.; Chen, R. Size-dependent photoluminescence blinking mechanisms and volume scaling of biexciton Auger recombination in single $CsPbI_3$ perovskite quantum dots. *J. Chem. Phys.* **2024**, *160*, 174505.
17. Bai, X.; Li, H.; Peng, Y.; Zhang, G.; Yang, C.; Guo, W.; Han, X.; Li, J.; Chen, R.; Qin, C.; et al. Role of aspect ratio in the photoluminescence of single CdSe/CdS dot-in-rods. *J. Phys. Chem. C* **2022**, *126*, 2699-2707.
18. Korepanov, O.; Kozodaev, D.; Aleksandrova, O.; Bugrov, A.; Firsov, D.; Kirilenko, D.; Mazing, D.; Moshnikov, V.; Shomakhov, Z. Temperature- and size-dependent photoluminescence of $CuInS_2$ quantum dots. *Nanomaterials* **2023**, *13*, 2892.
19. Dong, Y.; Qiao, T.; Kim, D.; Parobek, D.; Rossi, D.; Son, D.H. Precise control of quantum confinement in cesium lead halide perovskite quantum dots via thermodynamic equilibrium. *Nano Lett.* **2018**, *18*, 3716-3722.
20. Larson, H.; Cossairt, B.M. Indium-poly (carboxylic acid) ligand interactions modify InP quantum dot nucleation and growth. *Chem. Mater.* **2023**, *35*, 6152-6160.
21. Paik, T.; Greybush, N.J.; Najmr, S.; Woo, H.Y.; Hong, S.V.; Kim, S.H.; Lee, J.D.; Kagan, C.R.; Murray, C.B. Shape-controlled synthesis and self-assembly of highly uniform upconverting calcium fluoride nanocrystals. *Inorg. Chem. Front.* **2024**, *11*, 278-285.
22. Chen, J.; Zhang, L.; Li, S.; Jiang, F.; Jiang, P.; Liu, Y. Cu-deficient cuinse quantum dots for "turn-on" detection of adenosine triphosphate in living cells. *ACS Appl. Nano Mater.* **2021**, *4*, 6057-6066.
23. Akkerman, Q.A.; Park, S.; Radicchi, E.; Nunzi, F.; Mosconi, E.; De Angelis, F.; Brescia, R.; Rastogi, P.; Prato, M.; Manna, L. Nearly monodisperse insulator Cs_4PbX_6 (X= Cl, Br, I) nanocrystals, their mixed halide compositions, and their transformation into $CsPbX_3$ nanocrystals. *Nano Lett.* **2017**, *17*, 1924-1930.
24. Kirakosyan, A.; Kim, Y.; Sihn, M.R.; Jeon, M.G.; Jeong, J.R.; Choi, J. Solubility-controlled room-temperature synthesis of cesium lead halide perovskite nanocrystals. *ChemNanoMat* **2020**, *6*, 1863-1869.
25. Manoli, A.; Papagiorgis, P.; Sergides, M.; Bernasconi, C.; Athanasiou, M.; Pozov, S.; Choulis, S.A.; Bodnarchuk, M.I.; Kovalenko, M.V.; Othonos, A. Surface functionalization of $CsPbBr_3$ nanocrystals for photonic applications. *ACS Appl. Nano Mater.* **2021**, *4*, 5084-5097.
26. Yong, Z.; Guo, S.; Ma, J.; Zhang, J.; Li, Z.; Chen, Y.; Zhang, B.; Zhou, Y.; Shu, J.; Gu, J.; et al. Doping-enhanced short-range order of perovskite nanocrystals for near-unity violet luminescence quantum yield. *J. Am. Chem. Soc.* **2018**, *140*, 9942-9951.
27. Li, J.; Wang, D.; Zhang, G.; Yang, C.; Guo, W.; Han, X.; Bai, X.; Chen, R.; Qin, C.; Hu, J.; et al. The role of surface charges in the blinking mechanisms and quantum-confined stark effect of single colloidal quantum dots. *Nano Res.* **2022**, *15*, 7655-7661.
28. Li, B.; Gao, Y.; Wu, R.; Miao, X.; Zhang, G. Charge and energy transfer dynamics in single colloidal quantum dots/monolayer MoS_2 heterostructures. *Phys. Chem. Chem. Phys.* **2023**, *25*, 8161-8167.

29. Bi, C.; Wang, S.; Li, Q.; Kershaw, S.V.; Tian, J.; Rogach, A.L. Thermally stable copper(II)-doped cesium lead halide perovskite quantum dots with strong blue emission. *J. Phys. Chem. Lett.* **2019**, *10*, 943-952.
30. Mir, W.J.; Mahor, Y.; Lohar, A.; Jagadeeswararao, M.; Das, S.; Mahamuni, S.; Nag, A. Postsynthesis doping of Mn and Yb into $CsPbX_3$ (X = Cl, Br, or I) perovskite nanocrystals for downconversion emission. *Chem. Mater.* **2018**, *30*, 8170-8178.
31. Pradeep, K.R.; Viswanatha, R. Doped or not doped? importance of the local structure of Mn (II) in Mn doped perovskite nanocrystals. *Mater. Res. Bull.* **2021**, *141*, 111374.
32. Liu, W.; Lin, Q.; Li, H.; Wu, K.; Robel, I.; Pietryga, J.M.; Klimov, V.I. Mn^{2+}-doped lead halide perovskite nanocrystals with dual-color emission controlled by halide content. *J. Am. Chem. Soc.* **2016**, *138*, 14954-14961.
33. Yun, R.; Yang, H.; Sun, W.; Zhang, L.; Liu, X.; Zhang, X.; Li, X. Recent advances on Mn^{2+}-doping in diverse metal halide perovskites. *Laser Photonics Rev.* **2023**, *17*, 2200524.
34. Hu, F.; Zhang, H.; Sun, C.; Yin, C.; Lv, B.; Zhang, C.; Yu, W.W.; Wang, X.; Zhang, Y.; Xiao, M. Superior optical properties of perovskite nanocrystals as single photon emitters. *ACS Nano* **2015**, *9*, 12410-12416.
35. Han, X.; Zhang, G.; Li, B.; Yang, C.; Guo, W.; Bai, X.; Huang, P.; Chen, R.; Qin, C.; Hu, J. Blinking mechanisms and intrinsic quantum-confined stark effect in single methylammonium lead bromide perovskite quantum dots. *Small* **2020**, *16*, 2005435.
36. Yang, C.; Li, Y.; Hou, X.; Zhang, M.; Zhang, G.; Li, B.; Guo, W.; Han, X.; Bai, X.; Li, J. Conversion of photoluminescence blinking types in single colloidal quantum dots. *Small* **2023**, *20*, 2309134.
37. Podshivaylov, E.A.; Kniazeva, M.A.; Tarasevich, A.O.; Eremchev, I.Y.; Naumov, A.V.; Frantsuzov, P.A. A quantitative model of multi-scale single quantum dot blinking. *J. Mater. Chem.* **2023**, *11*, 8570-8576.
38. Yuan, G.; Gómez, D.E.; Kirkwood, N.; Boldt, K.; Mulvaney, P. Two mechanisms determine quantum dot blinking. *ACS Nano* **2018**, *12*, 3397-3405.
39. Li, B.; Zhang, G.; Yang, C.; Li, Z.; Chen, R.; Qin, C.; Gao, Y.; Huang, H.; Xiao, L.; Jia, S. Fast recognition of single quantum dots from high multi-exciton emission and clustering effects. *Opt. Express* **2018**, *26*, 4674.
40. Bi, C.; Wang, S.; Li, Q.; Kershaw, S.V.; Tian, J.; Rogach, A.L. Thermally stable copper (II)-doped cesium lead halide perovskite quantum dots with strong blue emission. *J. Phys. Chem. Lett.* **2019**, *10*, 943-952.
41. Nair, G.; Zhao, J.; Bawendi, M.G. Biexciton quantum yield of single semiconductor nanocrystals from photon statistics. *Nano Lett.* **2011**, *11*, 1136-1140.
42. Guo, W.; Tang, J.; Zhang, G.; Li, B.; Yang, C.; Chen, R.; Qin, C.; Hu, J.; Zhong, H.; Xiao, L.; et al. Photoluminescence blinking and biexciton Auger recombination in single colloidal quantum dots with sharp and smooth core/shell interfaces. *J. Phys. Chem. Lett.* **2021**, *12*, 405-412.
43. Park, Y.; Bae, W.K.; Padilha, L.A.; Pietryga, J.M.; Klimov, V.I. Effect of the core/shell interface on Auger recombination evaluated by single-quantum-dot spectroscopy. *Nano Lett.* **2014**, *14*, 396-402.
44. Zhuang, X.; Liang, B.; Jiang, C.; Wang, S.; Bi, H.; Wang, Y. Narrow band organic emitter for pure green solution-processed electroluminescent devices with CIE coordinate y of 0.77. *Adv. Opt. Mater.* **2024**, *12*, 2400490.
45. Li, S.; Pan, J.; Yu, Y.; Zhao, F.; Wang, Y.; Liao, L. Advances in solution-processed blue quantum dot light-emitting diodes. *Nanomaterials* **2023**, *13*, 1695.
46. Kumar, S.; Jagielski, J.; Kallikounis, N.; Kim, Y.; Wolf, C.; Jenny, F.; Tian, T.; Hofer, C.J.; Chiu, Y.; Stark, W.J.; et al. Ultrapure green light-emitting diodes using two-dimensional formamidinium perovskites: achieving recommendation 2020 color coordinates. *Nano Lett.* **2017**, *17*, 5277-5284.